# Thermo-Magneto-Convective Transport around a Square Cylinder in a Square Duct under Strong Axial Magnetic Field

D. Chatterjee[1†] and S. K. Gupta[2]

[1] *Simulation & Modeling Laboratory, CSIR-Central Mechanical Engineering Research Institute, Durgapur-713209, India*
[2] *Department of Mechanical Engineering, Massachusetts Institute of Technology, 77 Massachusetts Avenue, Cambridge, Massachusetts 02139, USA*

†*Corresponding Author Email: rsdchat@yahoo.co.in*

## ABSTRACT

A quasi two-dimensional numerical study is performed to analyze the thermo-magneto-convective transport of liquid metal around a square cylinder in a square duct subjected to a strong externally imposed axial magnetic field. The channel bottom wall is considered heated while the top wall is maintained at the free stream temperature keeping the cylinder adiabatic. The Reynolds and Hartmann numbers are kept in the range $0 < \text{Re} \le 6000$ and $0 < \text{Ha} \le 2160$. The flow dynamics in the aforementioned range of parameters reveals the existence of four different regimes out of which the first three ones are similar to the classical non-MHD 2-D cylinder wakes while the fourth one is characterized by the vortices evolved from the duct side walls due to the boundary layer separation which strongly disturbs the Kármán vortex street. The flow dynamics and heat transfer rate from the heated channel wall are observed to depend on the imposed magnetic field strength. With increasing magnetic field, the flow becomes stabilized resulting in a degradation in the forced convection heat transfer. A special case at a very high Reynolds number $Re = 3 \times 10^4$ with $Ha = 2160$ is also considered to show the development of a Kelvin–Helmholtz-type instability that substantially affects the heat transfer rate.

**Keywords**: Square cylinder; MHD flow; Forced convection heat transfer; Axial magnetic field; Quasi two-dimensional model; Kelvin–Helmholtz- instability.

## NOMENCLATURE

| | | | |
|---|---|---|---|
| $a$ | height of the duct | $U$ | inlet velocity |
| $B$ | magnetic field strength | $u, v$ | dimensionless velocity components |
| $C_D$ | drag coefficient | $w$ | width of the duct |
| $C_L$ | lift coefficient | $x, y$ | dimensionless rectangular coordinates |
| $c_p$ | specific heat | **Greek symbols** | |
| $d$ | size of the cylinder | $\alpha$ | thermal diffusivity |
| $f$ | vortex shedding frequency | $\beta$ | blockage ratio |
| $Ha$ | Hartmann number | $\varepsilon$ | relative error |
| $L_d$ | downstream length | $\nu$ | kinematic viscosity |
| $L_u$ | upstream length | $\Theta$ | dimensionless temperature |
| $k$ | thermal conductivity of fluid | $\rho$ | density |
| $N$ | Stuart number | $\sigma$ | electrical conductivity |
| $Nu$ | Nusselt number | **Subscripts** | |
| $p$ | dimensionless pressure | $av$ | average |
| $Pr$ | Prandtl number | $c$ | critical |
| $Re$ | Reynolds number | $m$ | maximum |
| $St$ | Strouhal number | $w$ | cylinder surface |
| $T$ | temperature | $\infty$ | free-stream |

## 1. INTRODUCTION

The thermofluidic transport around solid objects are important because of its tremendous applications in diverse fields of engineering. The processes are fundamentally also important since the boundary layer separation might be the most intriguing phenomenon in fluid dynamics. The imposition of an external magnetic field to the transport of an electrically conducting fluid opens up a new realm of transport phenomena, the magnetohydrodynamics (MHD). The magnetic field interacts with the electrically conducting fluid to produce electromagnetic Lorentz force which is basically damping in nature. This causes a reduction in the turbulent intensity of the MHD flow, thereby affecting the thermofluidic transport significantly. In applications like nuclear fusion reactors, the liquid metal blankets are prone to such magnetic damping. Hence, there is a chance for the degradation of the heat transfer. The heat transfer can be augmented by promoting the turbulence by placing obstacles inside the blankets. However, the thermofluidic transport around the obstacles will strongly depend on the shape of the obstacles.

In MHD flows over bluff bodies, apart from the geometric shape of the body, the orientation of the magnetic field with respect to the body axis plays a crucial role. While the streamwise (Mutschke *et al.*, 1997, 2001; Yoon *et al.*, 2004) and transverse orientations (Hussam *et al.*, 2011, 2013; Chatterjee *et al.*, 2012, 2013a, b, 2014; Chutia and Deka, 2015) have received some attention, the axial orientation is very infrequent. Mück *et al.* (2000) carried out a three-dimensional numerical simulation of the MHD liquid metal flow around a square cylinder with an axially oriented magnetic field in a rectangular duct. Sommeria and Moreau (1982) proposed a quasi-two-dimensional model that assumes that the flow outside the Hartmann layers is nearly two-dimensional. Using the model in Sommeria and Moreau (1982), Dousset and Pothérat (2008) studied the quasi-two-dimensional flow of liquid metal in a square duct past a circular cylinder in presence of a strong axially imposed magnetic field. However, the heat transfer aspects were not taken into consideration in these studies.

As such, it has been observed that apart from the work of Chatterjee and Gupta (2015) nobody has reported till date the heat transfer aspect for liquid metal flow over square object placed in a heated duct under axially oriented strong magnetic field. This has got particular importance in nuclear engineering and electromagnetic casting. Accordingly, we emphasize here to understand the MHD thermal transport over a square object in a duct subjected to strong axial magnetic field.

## 2. MATHEMATICAL FORMULATION

We consider flow of an electrically conducting and incompressible fluid (an eutectic alloy, GaInSn) in a duct of square cross section past a square cylinder (Fig. 1). All the solid walls are assumed to be electrically insulated and the cylinder is thermally insulated as well. The cylinder axis is at the centre of the duct, and orthogonal to the streamwise direction. The bottom wall (in the equivalent 2-D problem, refer to Fig. 1(b)) is considered heated $(T_w)$ while the top wall (Fig. 1(b)) is kept at the free stream temperature $(T_\infty < T_w)$. The duct dimensions ($a = w = 0.04$ m) and the cylinder size ($d = 0.01$ m) are so chosen that it produces a blockage ratio $\beta = d/w = 0.25$. The upstream $(L_u)$ and the downstream $(L_d)$ lengths are chosen as $12d$ and $42d$ respectively. These values are in conformity with Dousset and Pothérat (2008). A steady homogeneous magnetic field B with intensities between 0 and 1.35 Tesla is imposed along the cylinder axis.

The quasi two-dimensional model described in Sommeria and Moreau (1982) is used here which is derived by averaging the flow equations along the direction of the magnetic field. The model is particularly valid for $Ha \gg 1$ and $N \gg 1$ ($N = Ha^2/\text{Re}$ is the interaction parameter). The dimensionless governing equations in absence of any phenomenological cross effects and neglecting natural convection, viscous dissipation and Joule heating can be stated as:

$$\nabla \cdot \mathbf{u} = 0, \tag{1}$$

$$\frac{\partial \mathbf{u}}{\partial t} + (\mathbf{u}.\nabla)\mathbf{u} = -\nabla p + \frac{1}{\text{Re}}\nabla^2\mathbf{u} - 2\frac{d^2}{a^2}\frac{Ha}{\text{Re}}\mathbf{u} \tag{2}$$

$$\frac{\partial \Theta}{\partial t} + (\mathbf{u}.\nabla)\Theta = \frac{1}{\text{Re}\,\text{Pr}}\nabla^2\Theta \tag{3}$$

where $\mathbf{u}$, $p$ and $\Theta$ are the dimensionless velocity, pressure and temperature fields, respectively, projected onto the *x-y* plane, *t* is the dimensionless time, $\text{Re} = u_m d/\nu$ is the Reynolds number (where the reference velocity $u_m$ is the maximum of the velocity profile imposed at the inlet boundary at $y = 0$), $Ha = aB\sqrt{\sigma/\rho\nu}$ is the Hartmann number with $\text{Pr} = \nu/\alpha$ being the Prandtl number ($\alpha = k/\rho c_p$ is the thermal diffusivity). The non-dimensional form of the model is obtained by scaling the lengths by the cylinder size $d$, pressure by $\rho u_m^2$, time by $d/u_m$ and temperature by $\Delta T = T_w - T_\infty$ The fluid properties are described by density $\rho = 6360$ kg m$^{-3}$, kinematic viscosity $\nu = 3.4 \times 10^{-7}$ m$^2$ s$^{-1}$, thermal conductivity $k = 16.5$ W m$^{-1}$ K$^{-1}$, specific heat $c_p = 152.6$ J kg$^{-1}$ K$^{-1}$ and electrical conductivity $\sigma = 3.46 \times 10^6$ Ω$^{-1}$ m$^{-1}$. The Prandtl number is obtained as $Pr = 0.02$. The flow is assumed to start impulsively from rest with a velocity $u_m$ everywhere in the domain.
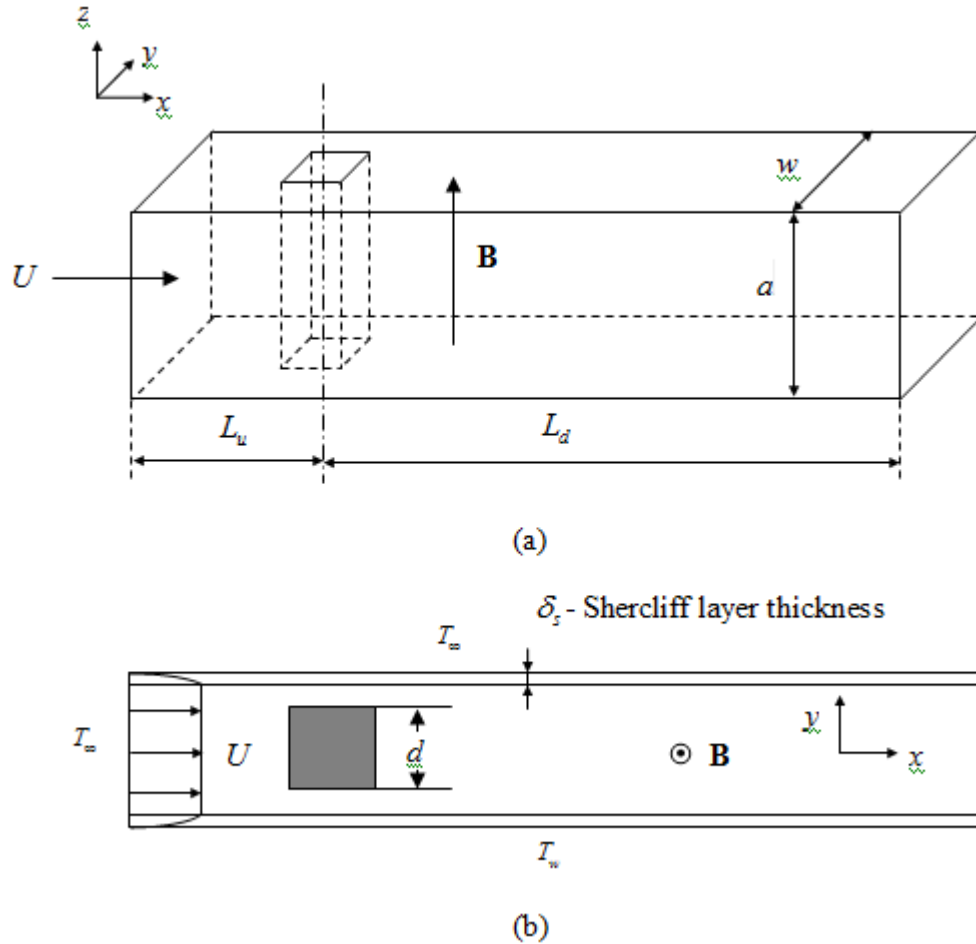
At the inlet ($x = -L_u$) the boundary condition is

(a)



(b)

**Fig. 1. (a) Actual configuration of the problem. (b) equivalent 2-D problem.**

derived as the exact parallel flow solution of Eqs. (1) and (2) for the duct flow problem without the obstacle given by:

$$U = u_m \left[ \frac{\cosh\left(yd\sqrt{2Ha}/a\right) - \cosh\left(h\sqrt{2Ha}/2a\right)}{1 - \cosh\left(h\sqrt{2Ha}/2a\right)} \right]$$

(4)

The exit boundary ($x = L_d$) is located sufficiently far downstream from the region of interest hence an outflow boundary condition is applied at the outlet. The outflow boundary condition is modeled by a homogeneous Neumann condition for the velocity and temperature variables as: $\partial_n \mathbf{u}|_{outlet} = 0$ and $\partial_n \Theta|_{outlet} = 0$. No slip boundary conditions are imposed on the side walls and on the cylinder surface ($\mathbf{u}|_{solid\ wall} = 0$). Temperatures at the inlet and top wall are set at $\Theta = (T - T_\infty)/(T_w - T_\infty) = 0$ and on the bottom wall $\Theta = 1$. The cylinder is thermally insulated (i.e. a zero normal temperature gradient is imposed on the cylinder surface, $\partial_n \Theta|_{cylinder} = 0$). Pressure boundary conditions are not explicitly required since the solver extrapolates the pressure from the interior.

## 3. NUMERICAL TECHNIQUE AND VERIFICATION

The conservation equations subjected to the aforementioned boundary conditions are solved using a finite volume based CFD solver Ansys Fluent (2010). Ansys Fluent solves the governing system of partial differential equations in a collocated grid system. The QUICK (Quadratic Upstream Interpolation Convective Kinetics) scheme is used for spatial discretization of the convective terms and a central difference scheme is used for the diffusive terms. A standard pressure interpolation scheme is used to compute the face values of pressure from the cell values. PISO (Pressure-Implicit with Splitting of Operators) algorithm is used as the pressure-velocity coupling scheme. A second order implicit time integration is used. The dimensionless time step size is taken as $\delta t = 2 \times 10^{-3}$. Finally, the algebraic equations are solved by using the Gauss-Siedel point-by-point iterative method in conjunction with the Algebraic Multigrid (AMG) method solver. The use of the AMG method in conjunction with the Gauss-Siedel type iterative technique can greatly accelerates the convergence and reduce the computational time. (Huang and Chang, 2003). The convergence criteria based on relative error for the inner (time step)

**Table 1 Grid sensitivity analysis showing characteristics of various meshes and errors in average drag coefficient and Strouhal number at *Re* = 100**

| Meshes | M1 | M2 | M3 | M4 | M5 |
|---|---|---|---|---|---|
| Total nodes on cylinder surface | 220 | 280 | 340 | 400 | 460 |
| Nodes in the Shercliff layers at the top and bottom walls for $Ha = 2160$ | 12 | 16 | 20 | 24 | 28 |
| Total nodes in the domain | 42400 | 71600 | 112000 | 155210 | 196200 |
| $\varepsilon_{C_D} = \left|1 - C_D\left(Mi\right)/C_D\left(M\,5\right)\right|$ | 0.058 | 0.046 | 0.0032 | 0.0030 | - |
| $\varepsilon_{St} = \left|1 - St\left(Mi\right)/St\left(M\,5\right)\right|$ | 0.006 | 0.009 | 0.00024 | 0.00022 | - |
| $\varepsilon_{Nu} = \left|1 - Nu\left(Mi\right)/Nu\left(M\,5\right)\right|$ | 0.062 | 0.052 | 0.044 | 0.042 | - |

iterations are set as $10^{-6}$ for the discretized equations. It is to be mentioned that due to the non-linearity of the convective terms in the governing equations, the problem is solved with a nested-loop approach. While so called global or inner iterations represent the real time-steps and are used to update the variables like velocity, temperature and pressure, based on a linearized system and boundary conditions; there is also an outer loop for updating the coefficients of the linearized system.

A non-uniform structured grid distribution having a close clustering of grid points in the vicinity of the cylinder wall is used. A very high grid density is adopted in the proximity of the object to capture the phenomena of flow suppression at the rear stagnation zone. Also in order to capture the Shercliff layers close clustering of grids is used near the walls. 100 divisions on each side of the square object are used with the first cell height from the cylinder as 0.513469 and 0.00366 from the duct wall. Altogether, 154125 cells (155210 nodes) are used to discretize the entire computational domain. Fig. 2 shows a representative grid distribution in the vicinity of the cylinder.
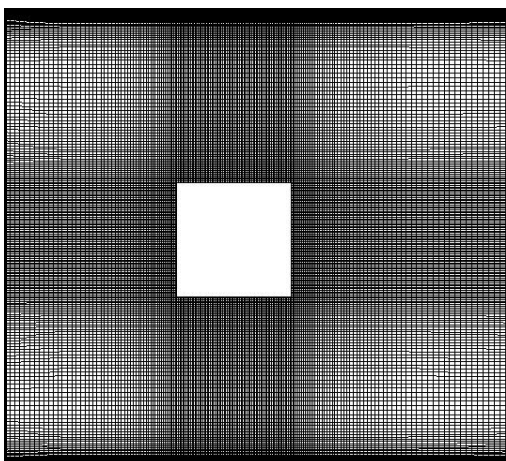


**Fig. 2. Closer view of the grid in the proximity of the cylinder.**

A comprehensive grid sensitivity analysis is also carried out to understand the self consistency of the problem. Table 1 shows the results of the grid

sensitivity analysis. Type (M4) mesh is preferred keeping in view the accuracy of the results and computational convenience in the simulations.

In an effort to numerically verify the adopted computational scheme, we compare the average drag coefficient and RMS lift coefficient obtained from the numerical simulation in Muck *et al.* (2000) for the MHD flow of liquid metal around a square obstacle in a duct with the present numerical technique. The comparison is shown in Fig. 3 with no significant discrepancies between the two sets of results.
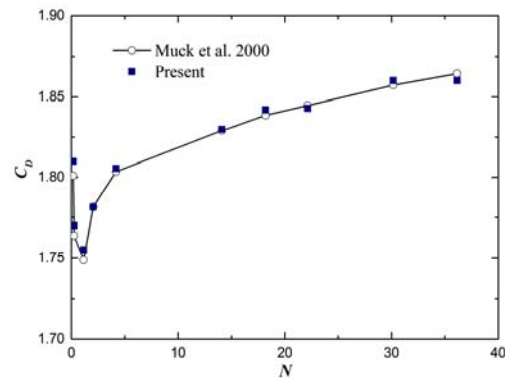


**(a)**
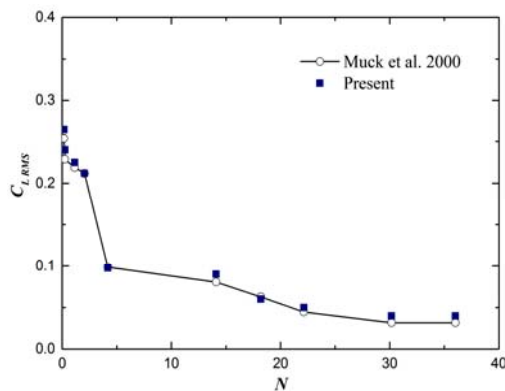


**(b)**

**Fig. 3. Comparative evolutions of $C_D$ (a) and $C_{L\,RMS}$ (b) vs. N. The comparison is made with the numerical results of Muck *et al.* (2000) ($\beta$ = 0.1) for *Re* = 200.**
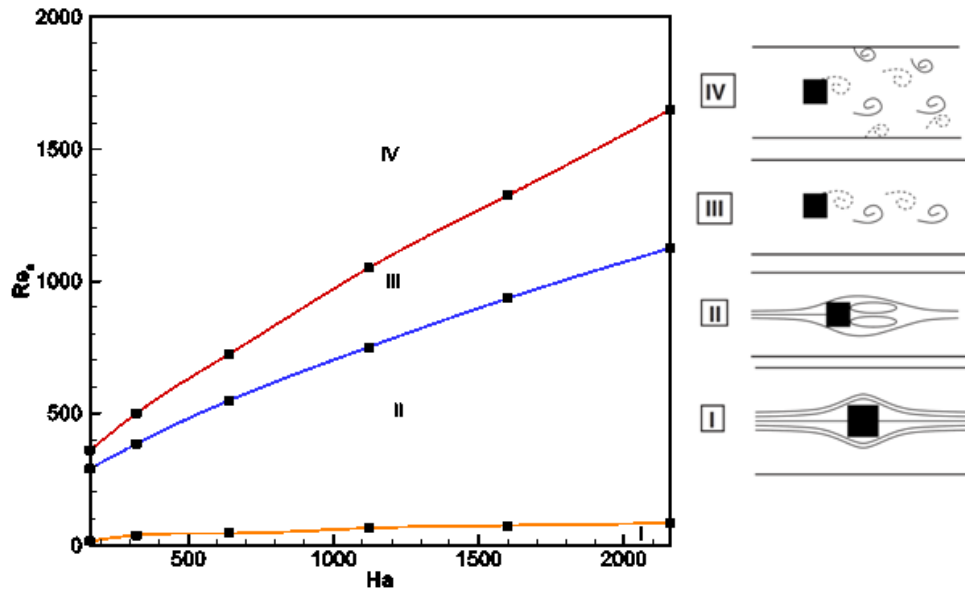
**Fig. 4. Flow regime map, Sector I: attached flow, sector II: steady symmetric recirculation region, sector III: laminar periodic flow with regular Kármán vortex street formation, and sector IV: flow regime where secondary vortices are emanated from the side walls.** $Re_c^I < Re_c^{II} < Re_c^{III}$ **are the successive critical thresholds between the flow regimes.**
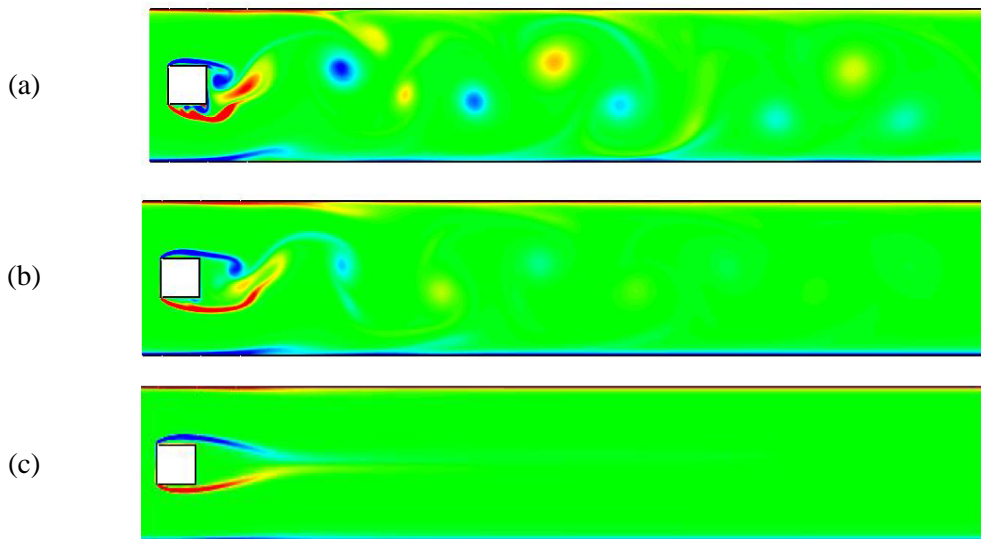


**Fig. 5. Dimensionless vorticity contours at a dimensionless time instant** $t = 100$ **and** $Re = 1000$ **for different Hartmann numbers (a)** $Ha = 320$, **(b)** $Ha = 1120$ **and (c)** $Ha = 2160$

## 4. RESULTS AND DISCUSSION

A series of numerical computations are performed fixing the blockage ratio $\beta = 0.25$ and taking B = 0.1, 0.2, 0.4, 0.7, 1.0, 1.35 Tesla corresponding to the Hartmann numbers $Ha$ = 160, 320, 640, 1120, 1600, 2160. In order to ensure that the quasi-two-dimensionality approximation remains valid, we intentionally choose $N \gg 1$ (say, $N = 10$). Hence, we start from $Ha = 160$ which is consistent with the choice of $N$.

### 4.1. Flow Dynamics

The typical flow regime map is presented in Fig. 4 showing clearly the four different regimes evolved

as an outcome of the imposed magnetic field. For a given magnetic field strength ($Ha$) as $Re$ increases gradually, four different regimes evolve. The first three regimes are identical to the 2-D non-MHD flow regimes, i.e., the attached flow regime I, the twin vortex regime II and the laminar periodic regime with regular Kármán vortex shedding III. The fourth regime IV is different from the non-MHD flow regime where the regular Kármán vortex street becomes irregular.

For a visual appreciation of the various flow regimes evolved, the instantaneous vorticity (dimensionless) contours are presented in Fig. 5 at a representative Reynolds number and for different Hartmann numbers. It is observed that in (a) regular
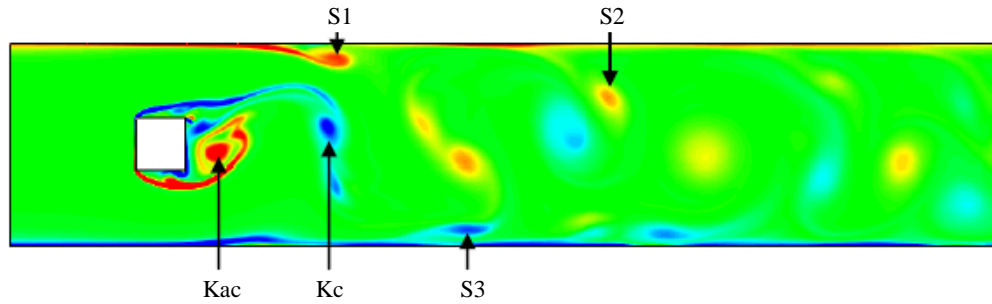
**Fig. 6. Regime IV: dimensionless vorticity contours at *t* = 60 for *Re* = 2000, *Ha* = 640. S1, S2 and S3 are secondary vortices, Kc and Kac are the clockwise and anticlockwise Kármán vortices.**

Kármán vortex street becomes irregular (regime IV), (b) regular Kármán vortex shedding is observed (regime III) and (c) flow becomes steady with twin vortex formation (regime II). The increasing magnetic field strength stabilizes the flow resulting in the suppression of vortex shedding.

As demonstrated in Fig. 6, the regime IV is characterized by the formation of the regular Kármán vortices (Kc and Kac) from the rolling-up of the free shear layers as in regime III along with the formation of the secondary vortices (S1, S2 and S3) from the separation of the Shercliff layer at the side walls. These secondary vortices either cross the downstream wake obliquely and interact strongly with the adjacent Kármán vortices or quickly dissipate as soon as they detach from the Shercliff layer (Mück *et al.*, 2000)

The particular role of the secondary vortices evolved from the side walls can be ascertained from Fig. 7 where the variation of the Strouhal frequency ( $St = f\,d/u_m$ , $f$ being the vortex shedding frequency) with Hartmann number for a representative Reynolds number $Re = 1000$ is shown. The frequency is observed to drop to zero in regime II where the flow becomes steady. Another drop in the frequency can be observed in regime IV which is attributable to the fact that in regime IV a secondary vortex develops in the Shercliff layer, it sheds and begins to cross the wake during its downstream motion, and creates an obstacle that impedes the flow of the incoming Kármán vortices. As a consequence, the vortex shedding frequency of the latter vortices decreases, leading to the observed drop in the Strouhal number. In regime III, as the formation of the secondary vortices occurs downstream of the cylinder, it does not affect that of the Kármán vortices.

Subsequently, an attempt has been made to delineate the characteristic features of the flow field qualitatively at a larger Reynolds and Hartmann numbers combination, $Re = 3 \times 10^4$ with $Ha = 2160$. The specific intention is to introduce a regime where instabilities take place in the free shear layers. Fig. 8 shows the instantaneous dimensionless vorticity contours depicting an irregular procession of counter-rotating vortices

whose formation mechanism was initiated by the Kelvin–Helmholtz (KH) instability. Small-scale vortices are generated in the free shear layers by the KH instability and feeds a chain of KH vortices. The latter roll up at the tail of the free shear layers, merge into a large vortex which eventually breaks away and flows downstream. This mechanism is alternately generated by either free shear layer and feeds the vortex street.
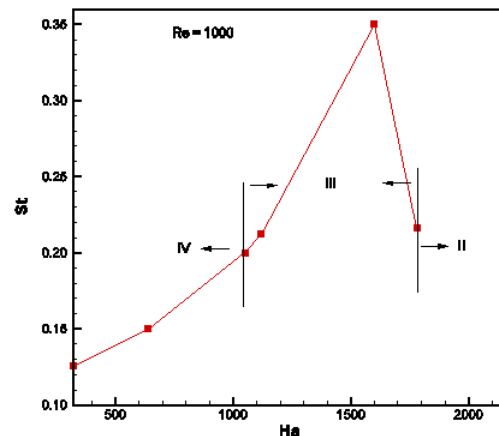


**Fig. 7. Strouhal frequency as a function of Hartmann number for *Re* = 1000.**

## 4.2. Thermal Characteristics

The instantaneous thermal fields are shown for different Hartmann numbers at $Re = 1000$ in Fig. 9. At this Reynolds number for low magnetic field strength $Ha = 320$ and 1120, the temperature fields are found time dependent since the flow is unsteady periodic with vortex shedding. However, with further increase in the magnetic field strength ($Ha = 2160$), the damping action of the magnetic field reduces the flow velocity near the heated wall resulting the suppression of the unsteadiness in the flow. The flow becomes steady at this *Ha*. This causes increase in the thermal boundary layer thickness and hence the temperature gradient along the heated wall decreases. The thermal field for $Re = 3 \times 10^4$ and $Ha = 2160$ is shown in Fig. 10. The KH instability at this regime makes the energy transport more chaotic. Accordingly, the heat
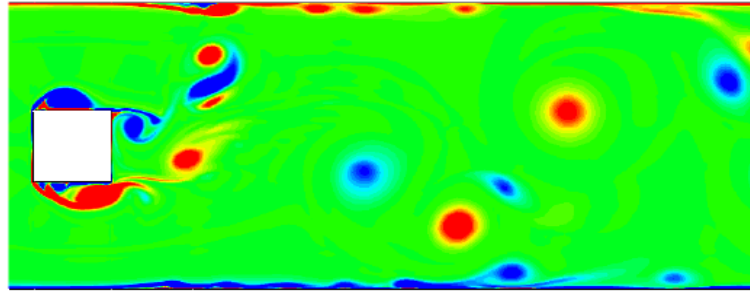
**Fig. 8. Dimensionless vorticity contours at** $Re = 3 \times 10^4$ **with *Ha* = 2160 showing Kelvin–Helmholtz (KH) instability**
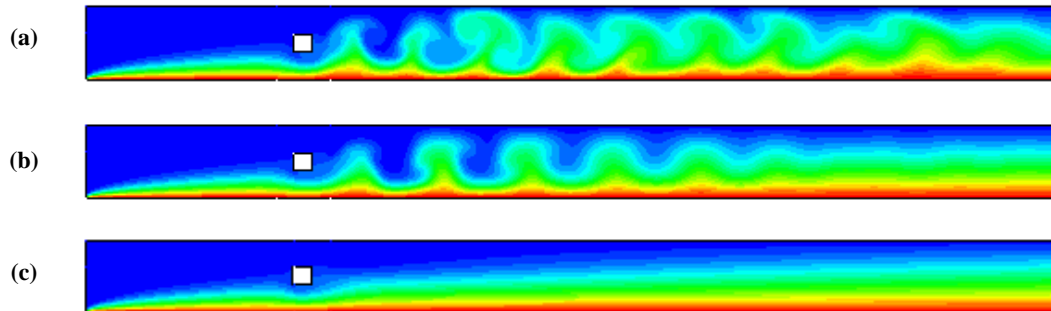


**Fig. 9. Dimensionless temperature contours at a dimensionless time instant *t* = 100 and *Re* = 1000 for different Hartmann numbers (a) *Ha* = 320, (b) *Ha* = 1120 and (c) *Ha* = 2160.**
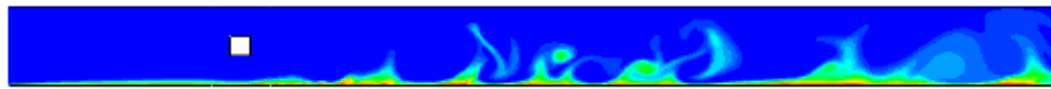


**Fig. 10. Dimensionless temperature contours at** $Re = 3 \times 10^4$ **with *Ha* = 2160.**

transfer rate increases significantly. It should be noted that at such *Re*, the small structures after the initial growth phase may become strongly 3-D and the quasi 2-D model can hardly provide more than some qualitative information on the 2-D dynamics of the more complex 3-D flow. In order to understand the heat transfer behavior in various regimes, the average Nusselt number of the heated bottom wall is presented in Table 2 for a specific Hartmann number (*Ha* = 2160). The table suggests that the heat transfer rate increases as we move on from regime I onwards. At regime I where the thermal transport is mainly dominated by diffusion, the heat transfer rate is substantially low. It increases gradually as the convective transport becomes slowly significant from the steady regime (II) towards unsteady vortex shedding regime (III). In regime IV, the heat transfer becomes high due to the interaction of the secondary vortices with the Kármán vortices. Finally, in the regime where the KH instability develops, the heat transfer becomes significantly high.

Fig. 11 shows the distribution of the instantaneous (at *t* = 100) local Nusselt number along the heated wall as a function of the streamwise coordinate for different Hartmann numbers at $Re = 10^3$ and $Re = 3 \times 10^4$. For the fixed Reynolds number, the

effect of Hartmann number on the heat transfer rate from the bottom heated wall can only be visible behind the cylinder. The flow is not changing at the upstream of the cylinder with Hartmann number and hence the heat transfer does not change. Downstream of the cylinder the flow shows substantial dependence on the Hartmann number. The shedding phenomena causes the local Nusselt number to fluctuate along the heated wall. With increasing magnetic field strength the flow instability is suppressed and accordingly the amplitude of fluctuation of the Nusselt number decreases and at higher Hartmann number when the flow becomes completely steady there is no fluctuation in the Nusselt number. When the Reynolds number is high, $Re = 3 \times 10^4$, the heat transfer rate becomes substantially high as a result of higher convective transport. Behind the cylinder, the Nusselt number shows large oscillation due to the existence of the KH instability.

The variation of the time and surface averaged heat transfer from the heated bottom wall with Reynolds number for different Hartmann numbers is presented in Fig. 12. The average Nusselt number increases monotonically with Reynolds number and with increasing Hartmann number it decreases. With increasing Reynolds number, the flow velocity

near the heated wall increases. Accordingly, the cold fluid is transported toward the hot region of the channel and the hot fluid near the heated wall is convected away to mix with the cold fluid. Consequently, the heat transfer is enhanced at larger Reynolds number. The dependence on Hartmann number is visible only at larger Reynolds number. At larger Hartmann number, thicker thermal boundary layer develops which causes the temperature gradient to decrease resulting in a corresponding decrease in the Nusselt number. The heat transfer rate is observed to increase substantially at larger Reynolds number as can be seen for $Re = 3 \times 10^4$ and $Ha = 2160$.

**Table 2 Heat transfer from heated wall for various regime**

|  | $Re$ | $Nu_{av}$ |
|---|---|---|
| Regime I | 84 | 0.3242 |
| Regime II | 500 | 0.5041 |
| Regime III | 1200 | 0.8860 |
| Regime IV | 2000 | 1.1841 |
| KH instability | $3 \times 10^4$ | 10.4538 |
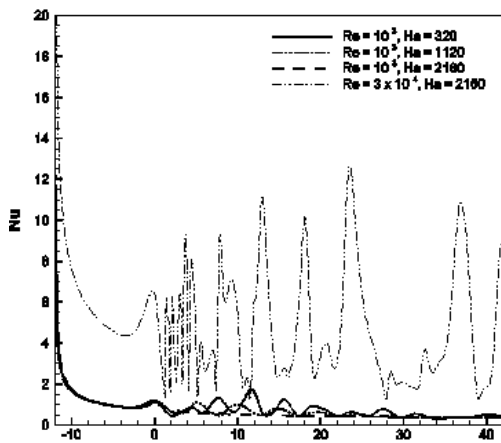


**Fig. 11. Distribution of the local Nusselt number on the heated bottom wall of the channel as a function of streamwise coordinate for different Hartmann numbers.**
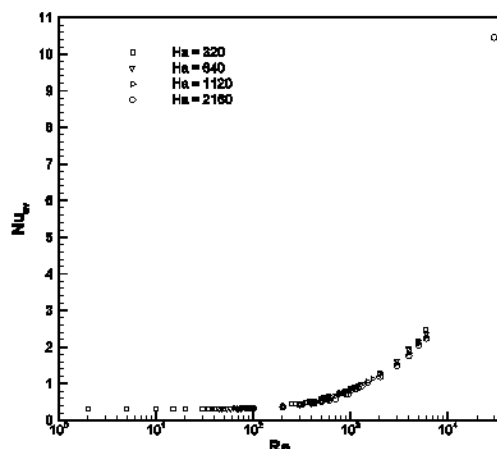


**Fig. 12. Variation of time and surface average Nusselt number of the heated bottom channel wall with Reynolds number for different Hartman numbers.**

## 5.  CONCLUSION

We perform a quasi two-dimensional simulation of the MHD flow and heat transfer of liquid metal in a square duct in presence of a square cylinder and a strong axially imposed external magnetic field. A wide variation of the Reynolds and Hartmann numbers are considered keeping the blockage ratio fixed. Additionally, computation at a larger Reynolds and Hartmann number combination is also performed to establish the Kelvin–Helmholtz instability occurring in the free shear layers. A finite volume based solver is used for the numerical computation after satisfactory validation.

The work essentially discusses in a concise manner the evolved flow dynamics along with the identification of various flow regimes originated as a result of the imposed magnetic field and the thermal transport behavior under the prevailing conditions. Four different regimes are identified out of which the first three are similar to the classical non-MHD regimes with a fourth one characteristically different from the non-MHD flow. This fourth regime is characterized by the interaction of the vortices emanated from the side walls (Shercliff layer) with the regular Kármán vortices. Due to such interaction the resulting vortex structure becomes highly irregular. Additionally, a special regime is observed at a larger Reynolds number where a Kelvin–Helmholtz (KH) type instability is taking place in the free shear layers. The role of the magnetic field is to stabilize the flow along with degradation in the heat transfer. Most importantly, the imposed magnetic field due to its damping nature actually shifts the appearance of the flow instabilities to higher *Re* values and the resulting flow regimes span over a wider range of *Re* than in comparison to the corresponding non-MHD cases. A drop in the Strouhal frequency is observed in the regime **IV** due to the impeding action of the secondary vortices originated in the Shercliff layer over the regular Kármán vortices. The frequency identically becomes zero at larger Hartmann number also when the shedding is completely suppressed. Finally, the heat transfer rate from the heated channel wall increases monotonically with Reynolds number and decreases with increasing Hartmann number. However, this dependence of heat transfer on Hartmann number is more profound at larger Reynolds number.

### REFERENCES

ANSYS Workbench User's Guide (2010). Release 13.0, ANSYS Inc., Canonsburg, PA.

Chatterjee, D. and K. Chatterjee (2013a). Unconfined flow and heat transfer around a square cylinder at low Reynolds and Hartmann numbers. *International Journal of Fluid Mechanics Research* 40, 71-90.

Chatterjee, D. and K. Chatterjee (2013b). Wall bounded flow and heat transfer around a circular cylinder at low Reynolds and

Hartmann numbers. *Heat Transfer-Asian Research* 42, 133-150.

Chatterjee, D. and S. K. Gupta (2015). MHD flow and heat transfer behind a square cylinder in a duct under strong axial magnetic field. *International Journal of Heat and Mass Transfer* 88, 1-13.

Chatterjee, D., K. Chatterjee and B. Mondal (2012). Control of flow separation around bluff obstacles by transverse magnetic field. *Journal of Fluids Engineering Transactions of ASME* 134, 091102-1-091102-11.

Chatterjee, D., K. Chatterjee, B. Mondal and N. B. Hui (2014). Wall confined flow and heat transfer around a square cylinder at low Reynolds and Hartmann numbers. *Heat Transfer-Asian Research* 43, 459-475.

Chutia, M. and P. Deka (2015). Numerical Study on MHD Mixed Convection Flow in a Vertical Insulated Square Duct with Strong Transverse Magnetic Field. *Journal of Applied Fluid Mechanics* 8, 473-481.

Dousset, V. and A. Pothérat (2008). Numerical simulations of a cylinder wake under a strong axial magnetic field. *Physics of Fluids* 20, 017104.

Huang, Z. H. and Q. S. Chang (2003). Gauss-Siedel type multigrid methods. *Journal of Computational Mathematics* 21, 421-434.

Hussam, W. K. and G. J. Sheard (2013). Heat transfer in a high Hartmann number MHD duct flow with a circular cylinder placed near the heated side-wall. *International Journal of Heat and Mass Transfer* 67, 944–954.

Hussam, W. K., M. C. Thompson and G. J. Sheard (2011). Dynamics and heat transfer in a quasi-two-dimensional MHD flow past a circular cylinder in a duct at high Hartmann number. *International Journal of Heat and Mass Transfer* 54, 1091-1100.

Mück, B., C. Günther, U. Müller and L. Bühler (2000). Three-dimensional MHD flows in rectangular ducts with internal obstacles. *Journal of Fluid Mechanics* 418, 265-295.

Mutschke, G., G. Gerbeth, V. Shatrov and A. Tomboulides (1997). Two- and three-dimensional instabilities of the cylinder wake in an aligned magnetic field. *Physics of Fluids* 9, 3114-3116.

Mutschke, G., G. Gerbeth, V. Shatrov and A. Tomboulides (2001). The scenario of three-dimensional instabilities of the cylinder wake in an external magnetic field. *Physics of Fluids* 13, 723-734.

Sommeria, J. and R. Moreau (1982). Why, how, and when, MHD turbulence becomes two-dimensional. *Journal of Fluid Mechanics* 118, 507-518.

Yoon, H. S., H. H. Chun, M. Y. Ha and H. G. Lee (2004). A numerical study on the fluid flow and heat transfer around a circular cylinder in an aligned magnetic field. *International Journal of Heat and Mass Transfer* 47, 4075-4087.